Morphological Characterization and Tribological Properties of TiCoNi Alloy Coatings on Ti–6Al–4V Alloy via Laser Deposition

Olanrewaju Seun Adesina[1,2] · Gabriel Ayokunle Farotade[2] · Babatunde Abiodun Obadele[3] · Olufemi Oluseun Sanyaolu[1] · Peter Pelumi Ikubanni[4] · Modupe Eunice Sanyaolu[5] · Adeolu Adesoji Adediran[4] · Adekunle Akanni Adeleke[6]

Abstract

The goal of this work is to improve the Ti–6Al–4V alloy's hardness and tribological behavior. Coaxial laser surface cladding was used to develop intermetallic layers of nickel (Ni), cobalt (Co), and titanium (Ti). Laser power of 900 W, beam spot size of 3 mm, powder feed rate of 1.0 g/min, and gas flow rate of 1.2 L/min are the optimized parameters used for laser depositions. The laser scan speeds were adjusted between 0.6 and 1.2 m/min. Investigations were conducted into the effects of powder admixture and laser parameters on the fabricated coatings' microstructure, tribological behavior and hardness. X-ray diffractometry (XRD), energy dispersive spectroscopy (EDS) with Scanning electron microscopy (SEM) was employed for the characterization of the microstructural evolution and phase identification, respectively. Additionally, the tribological experiment was conducted via UMT-2 –CETR reciprocating tribometer, and the coatings' micro-hardness characteristics were examined using EmcoTEST DURASCAN. The micrographs exhibit no signs of porousness, cracks, or stress introduction, according to the results. For every manufactured sample, good metallurgical adhesion was obtained. By comparing the hardness of the ternary coating (Co–Ni–10Ti deposited at a scan speed of 1.2 m/min, with a hardness of 980 HV) to the substrate (Ti–6Al–4V, with a hardness of 330 HV), a hardness increase of approximately 2.96 times was observed. Furthermore, the Co–Ni–10Ti coating, deposited at a scan speed of 1.2 m/min, demonstrated a 51.1% reduction in the coefficient of friction (COF) compared to the base alloy, indicating superior anti-wear performance. The enhanced properties are attributed to the formation of hard intermetallic compounds such as Ti–Co, Co_2Ti, Al_5Co_2, and Ni3Ti, along with their uniform distribution and finely tuned grain sizes.

Keywords Ti–6Al–4V alloy · Ti–Co–Ni powders · Material cladding · Hardness · Advanced manufacturing · Wear resistance · Microstructure

✉ Olanrewaju Seun Adesina
osaadesina@yahoo.com

1   Department of Mechanical Engineering, Redeemer's University, Ede, Nigeria

2   Department of Chemical, Metallurgical and Materials Engineering, Tshwane University of Technology, P.M.B. X680, Pretoria 0001, South Africa

3   Chemical, Materials & Metallurgical Engineering, Botswana International University of Science and Technology, Palapye, Botswana

4   Department of Mechanical Engineering, Landmark University, Omu-Aran, Nigeria

5   Department of Physical Science, Redeemer's University, Ede, Nigeria

6   Department of Mechanical Engineering, Nile University of Nigeria, Abuja, Nigeria

1 Introduction

Ti–6Al–4V alloy exhibits outstanding qualities that make it highly suitable for a range of engineering applications, including those in the automotive, marine, aerospace, and petrochemical industries. These attributes include good corrosion properties and its specific strength-to-weight ratio [1–5]. Due to its low hardness and poor wear resistance, Ti–6Al–4V alloy is only suitable for non-friction applications, despite its high strength making it suitable for components development for engineering purposes and in mechanical system's movable parts [6–9]. For instance, under contact load and relative motion, Titanium and its alloy-based technical materials are prone to breaking or denting on the surfaces [10].

Titanium alloys are increasingly used in industry. This is due to their excellent combination of high specific strength and heat resistance between 400 °C and 600 °C. These alloys exhibit great corrosion resistance in most cases [11], and due to their limited heat conductivity and tendency to fuse, titanium alloys are challenging to machine. Using a modern manufacturing technique called laser metal deposition, large, complicated items can be produced with little to no need for welding or machining [12].

Because titanium alloy is typically utilized in aerospace applications, the deposited pieces' fatigue qualities are crucial. A significant disadvantage of surface roughness is that it concentrates stress and creates sites for crack formation, which reduces fatigue performance [13]. It has been determined that the primary contributors to titanium's low tribological resistance and higher friction coefficient are linked to its crystal lattice-atomic structure, ability to resist plastic deformation, and the low tensile strength of the TiO_2 film which develops on the exterior part of the material [14–16].

The use of laser surface cladding to transform the surface of alloys is growing in popularity as a means of overcoming the limitations of Ti–6Al–4V alloy and not affecting the substrate bulk's characteristics [7, 17]. Consequently, the wear resistance and surface hardness of the Ti–6Al–4V alloy will significantly improve for new industrial applications [18, 19]. Laser cladding coatings have advantages over other surface modification methods like thermal spraying, cold spraying, physical vapor deposition (PVD) spraying, and magnetic sputtering. These advantages include dense microstructure, little thermal deformation, heat-affected zone (HAZ), and excellent metallurgical fusion of the metal alloy and materials for coating [20–22].

The microstructure and quality of the final product in laser metal deposition are influenced by various thermal phenomena, including maximum temperatures, temperature gradients, and cooling rates. To control the process, establish empirical property relationships, validate models, and gain insights, it is crucial to quantify and monitor these thermal responses [23–26].

Thermal monitoring in laser metal deposition assist to validate temperature-controlled microstructure models, reducing the need for extensive testing to optimize process parameters. Recent research indicates that slower travel speeds and higher laser power create longer melt pools and higher maximum temperatures. As the melt pool end moves, it hardens quickly and experiences maximum solid-phase cooling rates, which increase with travel velocity. [27].

The laser energy is transferred during laser metal deposition by conduction through the substrate and earlier layers, away from the melt pool. The remaining laser energy either contributes to the melting, superheating, and vaporization of the melt pool or spreads through convection and radiation to the surroundings.

Previous studies have shown that Ni–Co binary alloy coatings exhibit superior characteristics compared to monolithic coatings of either Co or Ni [28]. Based on previous studies by [29] and [30], Ti–Co intermetallic also has advantageous qualities like strong wear resistance and high hardness. However, the propensity to be defective (with pores and cracks) owing to thermal coefficient mismatch could be lessened. This could be achieved with nickel addition between the reinforced matrix of titanium and cobalt to serve as the binding phase. Moreover, it may be possible to promote the established ternary solubility of the binary phases of Ni–Ti and Co–Ti, which would lessen the likelihood that brittle intermetallics will form inside the coating matrix.

Ti–Co–Ni ternary alloy synthesis and characterization on the substrate Ti–6Al–4V alloy under variable clad composition and laser process parameters are the main focus of this research work. Furthermore, an investigation was conducted into the impact of parameters for processing on the surface morphology, microhardness, and tribological characteristics of the fused claddings. Ti–6Al–4V alloy is anticipated to form novel alloys having hard intermetallic interfaces and phase stability at high-temperature, which should exacerbate any wear and hardness issues brought on by the selection of a required system for ternary alloying. The Ti–Co–Ni alloys serve as reinforcing powdery materials. For meeting the needed extended service life as well as high strength, the intermetallic formation will significantly increase the value of hardness and substrate's (Ti–6Al–4V alloy) wear. This alloy may also be used as an alternative to coatings like chromium on metals for technology use [31].

2 Experiment

2.1 Materials and Process

Ti–6Al–4V (substrate) alloy was clad with titanium (Ti), cobalt (Co), and nickel (Ni) powders that were supplied by TSL Germany. The powders had a 99.9% purity and a particle size ranging between 45 and 95 μm. The morphological characteristics of the three powders as-received were analyzed using scanning electron microscope (SEM) equipped with an energy dispersive spectrometer (EDS), as shown in Fig. 1a–c. As expected for atomized powders, the microstructure of the cobalt, nickel, and titanium powders was found to be spherical. To enhance homogeneity, flowability, and prevent agglomeration-induced irregularities, powders of Ti, Co, and Ni were blended for 8 h at 49 rpm in a Tubular T2F mixer [32].

Before the laser cladding process, the substrate (Ti–6Al–4V alloy) (provided by a company in USA—TMS Titanium, Poway, California) was cut to 50×50×5 mm. The elemental constituents of the substrate are specified in Table 1. Prior
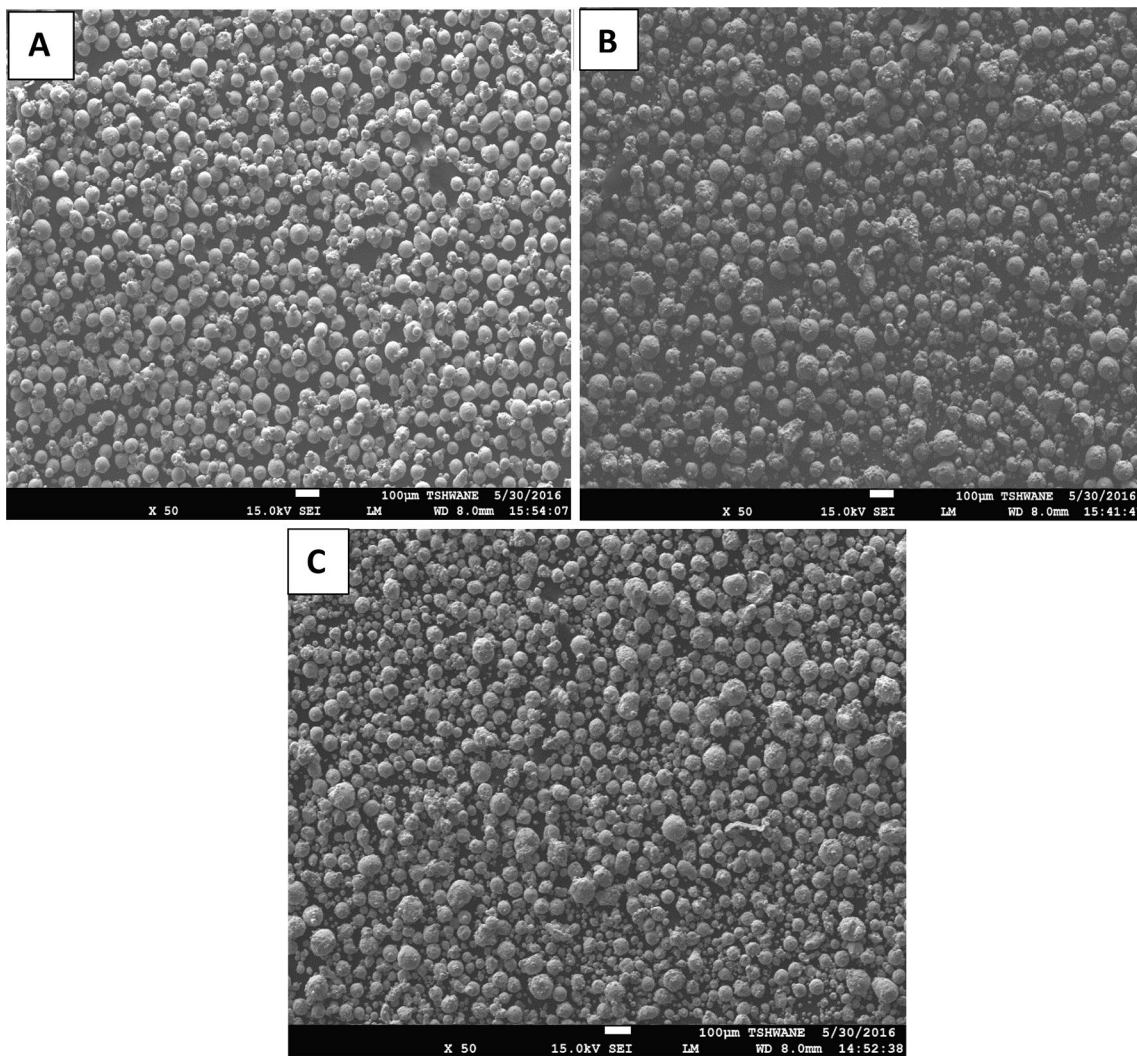
Fig. 1 Morphology of **a** Titanium **b** Cobalt and **c** Nickel powders

to this, silica grit was employed to sandblasted the substrate before acetone was used to clean it to improve the titanium alloy laser absorption and reduce reflection [33].

2.2 Laser Processing

Admixed powders of Ti–Co–Ni and Co–Ni–Ti (as presented in Table 2) were cladded on Ti–6Al–4V alloy using a YAG laser fitted with an articulated arm robotic system, utilizing the Continuous Wave 4.4 kW Rofin Sinar DY 044 Nd:YAG laser. The laser was operated at optimal settings

of laser power of 900 W, a beam spot size of 3 mm, a powder feed rate of 1.0 g/min, and a gas flow rate of 1.2 L/min, and scan speeds ranging from 0.6 to 1.2 m/min. Multiple clad tracks were deposited at a 45-degree angle to the substrate, with 50% overlap, to generate large surface area coatings. An inert atmosphere surrounding the molten pool was created during deposition by applying argon gas at a rate of 3 L/min. Considering titanium's strong affinity for oxygen, this was done to prevent oxidation. The laser cladding parameters used to deposit Ti–Co–Ni coatings on Ti–6Al–4V alloy were compiled in Table 2**.**

Table 1 Elemental constituents of the substrate (Ti–6Al–4V alloy)

N	O	C	Fe	V	Al	Ti
0.005	0.120	0.007	0.150	4.000	6.100	Balance

Table 2 Parameters utilized for the laser cladding of the TiCoNi ternary coatings

Sample	Clad material	Scan speed (m/min)	Power (W)	Powder feed rate (g/min)	Beam diameter (mm)	Gas flow (L/min)
A	TiCo–10Ni	0.6	900	1.0	1.0	1.2
B	TiCo–10Ni	1.2	900	1.0	1.0	1.2
C	CoNi–10Ti	0.6	900	1.0	1.0	1.2
D	CoNi–10Ti	1.2	900	1.0	1.0	1.2

2.3 Laser Coatings Characterization

Coatings for morphological examination were ground by employing grit SiC grinding papers (P80, P320, P1200, and P4000) on an automated diamond suspension dispenser equipped with a Struers TegraForce-25 after the laser cladding process. After grinding, the clad samples were refined with an MD-Chem OP-S polishing cloth and polished on an MD-Largo, both using a Diapro diamond suspension. The polished clad samples were then etched for about ten seconds in Kroll's reagent (92 ml H_2O, 6 ml HNO_3, and 2 ml HF) before being characterized. The etching was done to ensure that the unique microstructural phases were present.

The micrographs of the laser-clad coatings were studied using SEM (Model: JSM-7600F FE-SEM), and EDS was utilized to determine the elemental compositions. Intermetallic compounds were detected via an X-ray diffractometer (XRD) from Philips PW1713, which was outfitted with monochromatic CuKα radiation set at 40 kV and 20 mA. For the identification of the phase, the utilization of software with an in-built (ICSD) database and Philips Analytical X'Pert High Scores. With a step size of 0.02°, the scan ranges from 10° to 80° 2 theta (2θ).

2.4 Hardness Test

The clad samples micro-hardness profile was assessed at the interfacial regions of the coating–HAZ-substrate using the Vickers Hardness Tester EMCOTEST. This is to show how chilling and heat input affected the material characteristics throughout the corresponding areas. The indentation profile using Vickers hardness were made on the clad area surface toward the substrate for 10 s while the bearing load was 100 gf (0.98 N). After five distinct indents were made at nearby sections on the clad surface, a mean value was computed for each coating. This process is carried out on the coating's free surface as well as along each sample's longitudinal plane.

2.5 Tribological Test

Under dry sliding conditions, wear examinations were executed on the prepared Ti–6Al–4V coatings using UMT-2–CETR reciprocating tribometer, with a progressive analysis of the frictional coefficient values. With the help of the UMT-2-CETR tribometer apparatus, sliding action is possible while recording the friction coefficients for both strokes. A sample chuck was precisely fitted with specimens that had been cut to a 2 cm by 2 cm area, and the samples were then exposed to a downward vertical load. A tungsten carbide ball was used as the counterface, with a standard load of 15 N applied at a frequency of 5 Hz. The sliding speed was set to 2 m/s, the stroke length was 2 mm, and sliding time was 1000 s. The CERT UMT-2 tribometer software was used to obtain the experimental results that showed the frictional coefficient and wear depth on the material surfaces. Following the dry sliding wear test, the worn surfaces were inspected using a SEM to determine likely wear mechanism.

3 Results and Discussion

3.1 Morphological Examination of Ti–6Al–4V Substrate

Micrograph of the substrate with elemental constituents displayed via EDS is presented in Fig. 2. The substrate displays a good-structured texture surface with dispersed little whitish, and grayish scratches, as shown in the SEM image. The lamellar transformed β-phase are indicated by the whitish zones with a crystal structure of body centered cubic (BCC) while the hexagonal closed packed crystal structure (HCP) are indications of the primary α-phase (gray phase).

3.2 Microstructural Analyses of Laser Coatings

3.2.1 Interfacial Zone

The distinct microstructures of the Ti–Co–10Ni ternary claddings synthesized at two different laser scan speeds (0.6 and 1.2 m/min, respectively), are shown in Fig. 3A and B. The coatings' micrographs, the interfacial region, and the substrate alloy (Ti–6Al–4V) were all visible through observation. Due to varying cooling rates and scanning speeds, the fabricated coatings' microstructural evolution exhibits distinct characteristics. There were no visible pores or fractures at the interface, indicating a robust bonding metallurgically
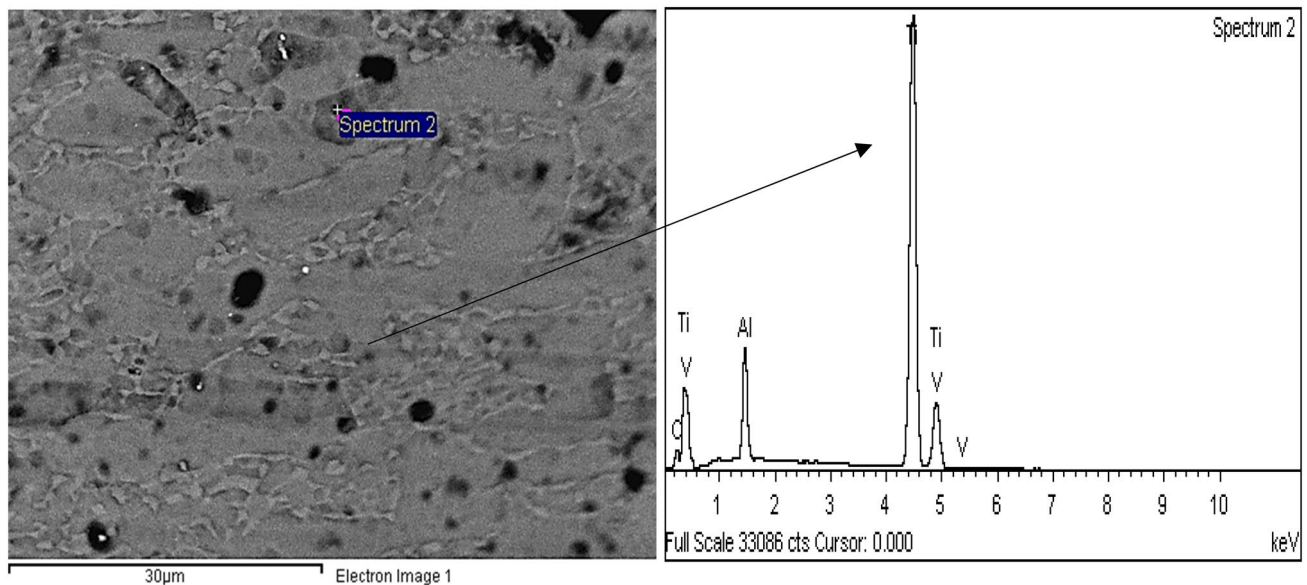
Fig. 2 SEM/EDS micrographs of Ti–6Al–4V alloy

between the substrate and the coating. The establishment of longer grains leads to micrographs and a larger HAZ region, as shown in Fig. 3A. This phenomenon is related to the solidification and dendritic structure formation. At lower laser scanning speed of 0.6 m/min, the periodic interaction of the laser and material rises owing to the available high energy density between the laser beam and melt pool.

Rapid cooling rate at high scan speed of 1.2 m/min resulted in a reduction of the substrate's absorbing energy and interaction time, as demonstrated in Fig. 3B [34]. A thinned dilution band in the HAZ is a consequence of the high cooling rate. Furthermore, quicker nucleation rates result in smaller grain sizes because there is less time for grain growth at higher cooling rates. In the micrograph of the coating, the evolution of grains or dendritic structures is influenced by temperature gradient and rate of solidification. According to a previous study by [35], the introduction of reinforcing material such as Co metallic powder is essentially important in dendrite formation. [36] showed that good wettability of Co causes melted powders to spread out and disperse on the substrate.

Point EDS analysis as presented in Fig. 3c and d indicate the presence of vanadium and aluminum (from the matrix material) as well as the alloying elements, Co, Ni, and Ti. This shows a significant interaction of the matrix material with the alloying elements in the melt pool [37].

In contrast, interfacial zones of the substrate and Co–Ni–10Ti coatings are shown in Fig. 4A and B at respective laser scan speeds of 0.6 and 1.2 m/min. The samples display similar crystal structure, free from pores, cracks, or micro-holes. Strong metallurgical adhesion was demonstrated in the interfacial zone, and imperfections like pores and cracks were absent. The grains in Fig. 4B are much finer than those in Fig. 4A. The interdiffusion of atoms caused by the fast solidification rate at high scan speeds could be the cause of the finely equiaxed dendrites shown in Fig. 4B. In the interface zone, the tendency for crack formation or stress initiation is eliminated when scanning at a high speed because there is insufficient period for the diffusion of these particles. The evolution of the crystal-like dendrite development is directed toward the substrate, as seen in Fig. 4A and B, where dendritic microstructures are evident. The outcomes exhibit distinctive morphological characteristics of multilayer synthetic coatings generated through laser cladding, owing to the thermal influence experienced during the laser scanning process. A larger interfacial zone is also produced by the cladding materials fusing with bigger sections of the substrate at low scan speeds, as depicted in Fig. 4A.

3.2.2 Laser Coatings Microstructural Analyses

The synthetic Ti–Co–10Ni coatings' microstructural evolution is shown in Fig. 5A and B at the two respective scan speeds. With no pores, cracks, or stress initiation, the two synthesized coatings produced equiaxed grains and dendrites as a mixture. Figure 5A displays coarse polygonal dendritic structures with larger grain sizes due to an extended interaction between the absorbing energy and the heated powders, which causes a slow rate cooling rate. In contrast, Fig. 5B shows the typical dendritic structure observed within clad layer, indicating a heat rapid transition during
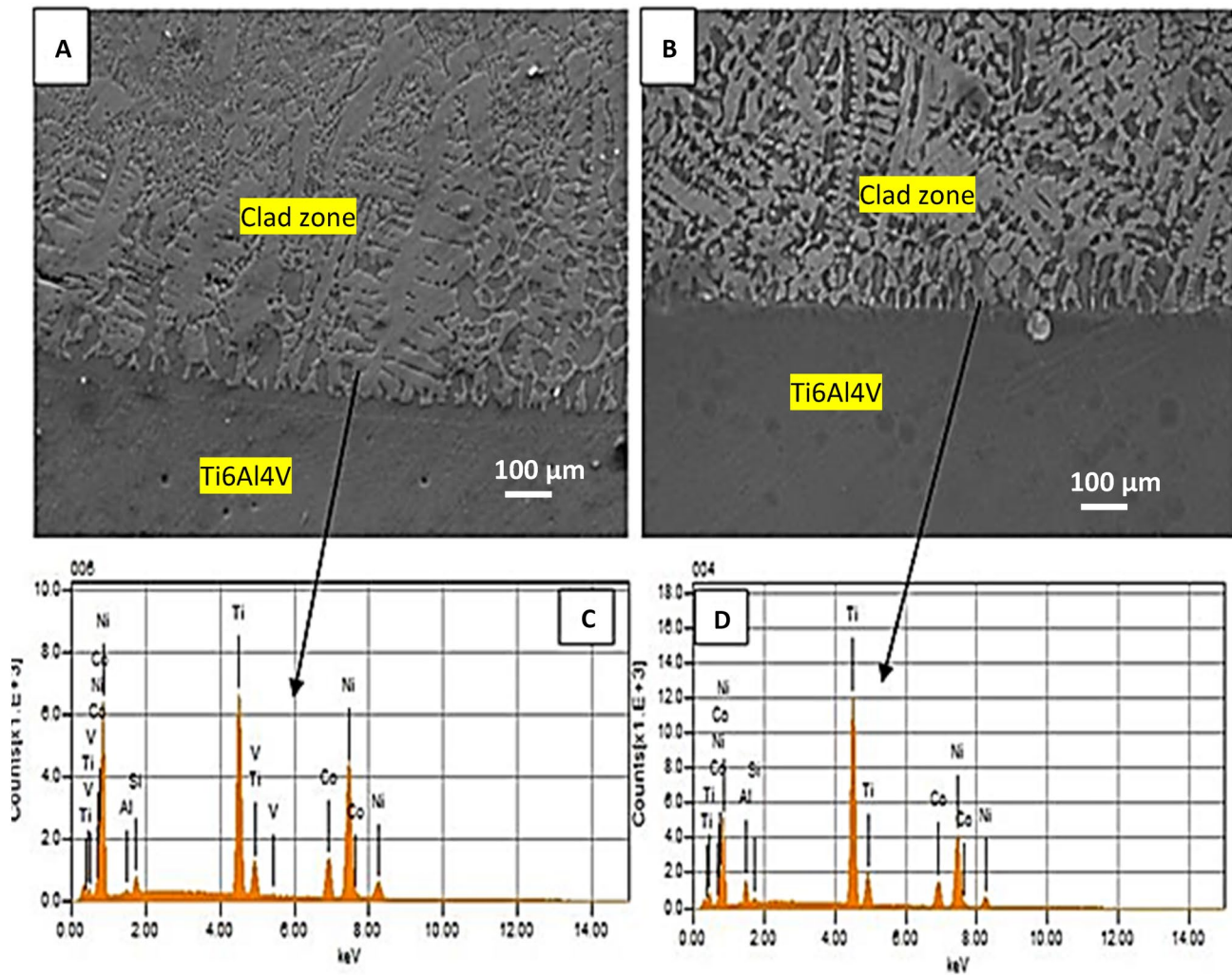
Fig. 3 SEM–EDS indicating interfacial zones of Ti–Co–10Ni clad samples at **A** 0.6 m/min and **B** 1.2 m/min

the solidification procedure [38, 39]. It clearly appears that the columnar grains have grown along with columnar grains. The variations in scan speeds could lead to the growth of distinct structures and distinct solidifying rates, which in turn cause variations in the microstructural development of the synthesized coatings [40]. Ti–Co, $TiCo_2$, and Co_3Ti and are the anticipated intermetallic phases which may be existing in the dendritic structures [37, 41–43]. Moreover, the introduction of nickel-based intermetallics like Ti_2Ni, NiTi, and Ni_3Ti as shown in XRD spectra (Fig. 7) is supported by the percentage of nickel reinforcement addition to the coatings' composition. This aligns with the research conducted by Cai et al. [44].

In contrast, the micrograph in Fig. 6A and B showed patterns with lave-like dendrites at the respective scan speeds. The formation of lave-like structures was caused by the atoms from the substrate and coating diffusing among themselves due to a high rate of solidification and temperature

difference. At lower scan speeds, precipitate diffusion led to larger dark grayish lave-like dendrites, while at higher scan speeds, insufficient diffusion resulted in white gray colored lave-like dendrites.

Based on the finding of Liu et al. [45], when a compound with a high Co–Ni content is heated to a high point, a laves phase is formed. Furthermore, dark, un-melted powder particles that had been deposited on the coating were visible in the SEM micrographs. [46] state that the laser beam's high convective effect is another factor that could hinder the powders at the substrate's free surfaces from melting completely.

3.3 Analyses of XRD of the Laser Coatings

The X-ray diffractometer phases of the ternary coatings of Ti–Co–10Ni (Fig. 7) and Co–Ni–10Ti (Fig. 8) which were developed at the two scan speeds, 0.6 and 1.2 m/min, are displayed. Both the laser scan speed and the composition of the
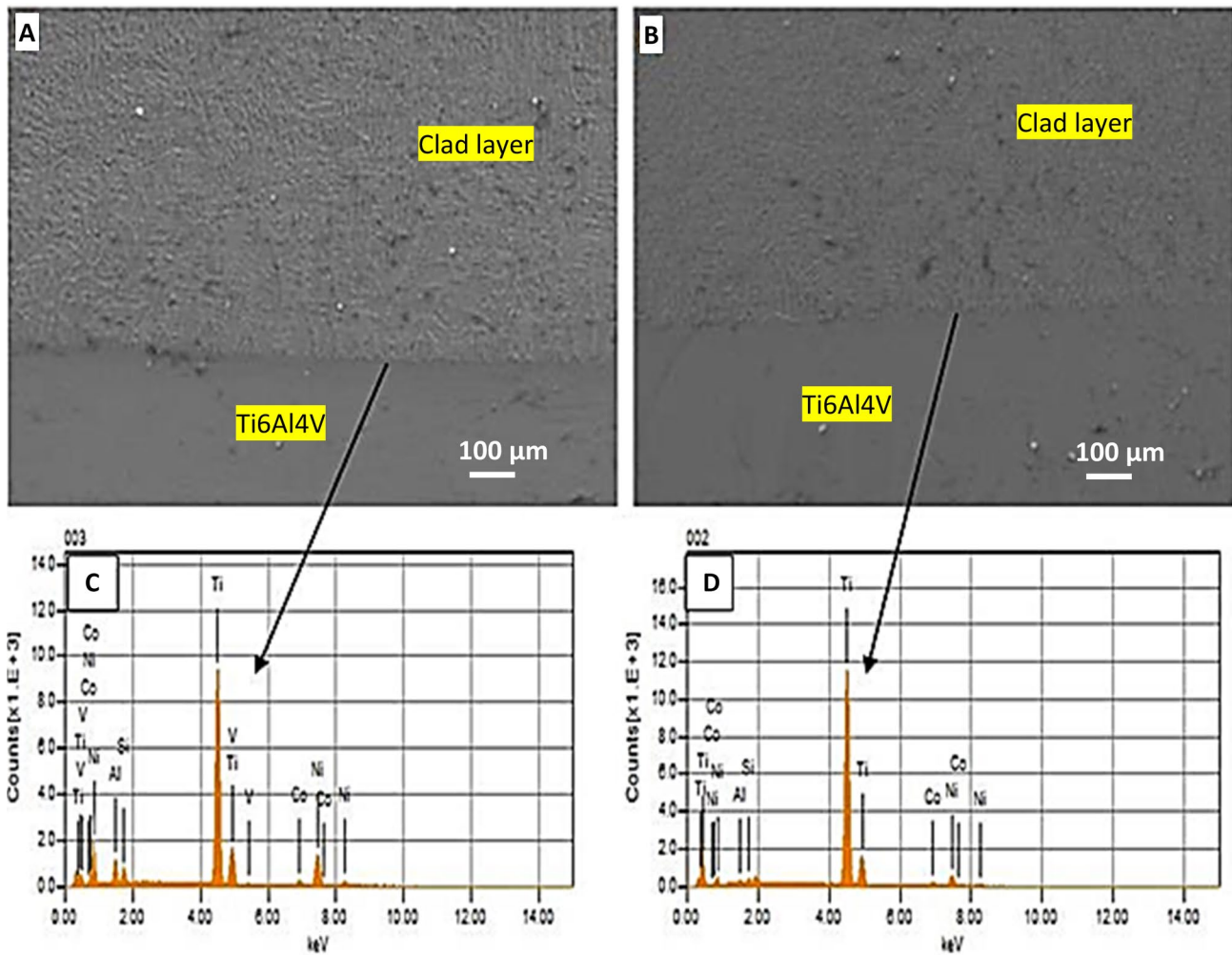
Fig. 4 SEM–EDS indicating interfacial zones of Co–Ni–10Ti clad samples at **A** 0.6 m/min and **B** 1.2 m/min
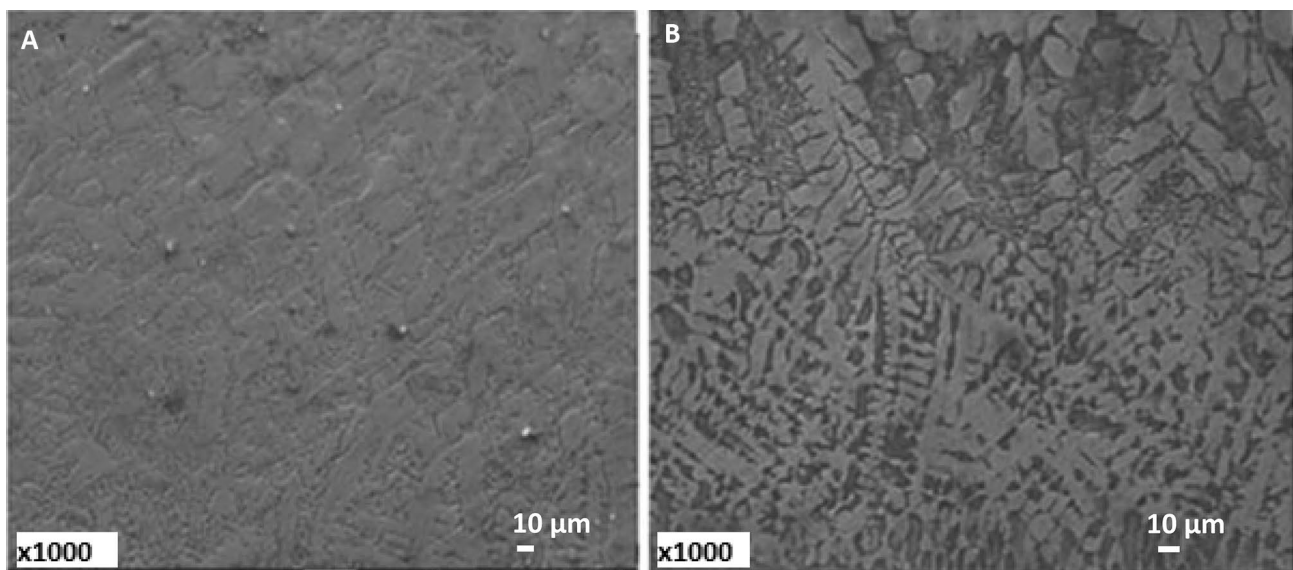

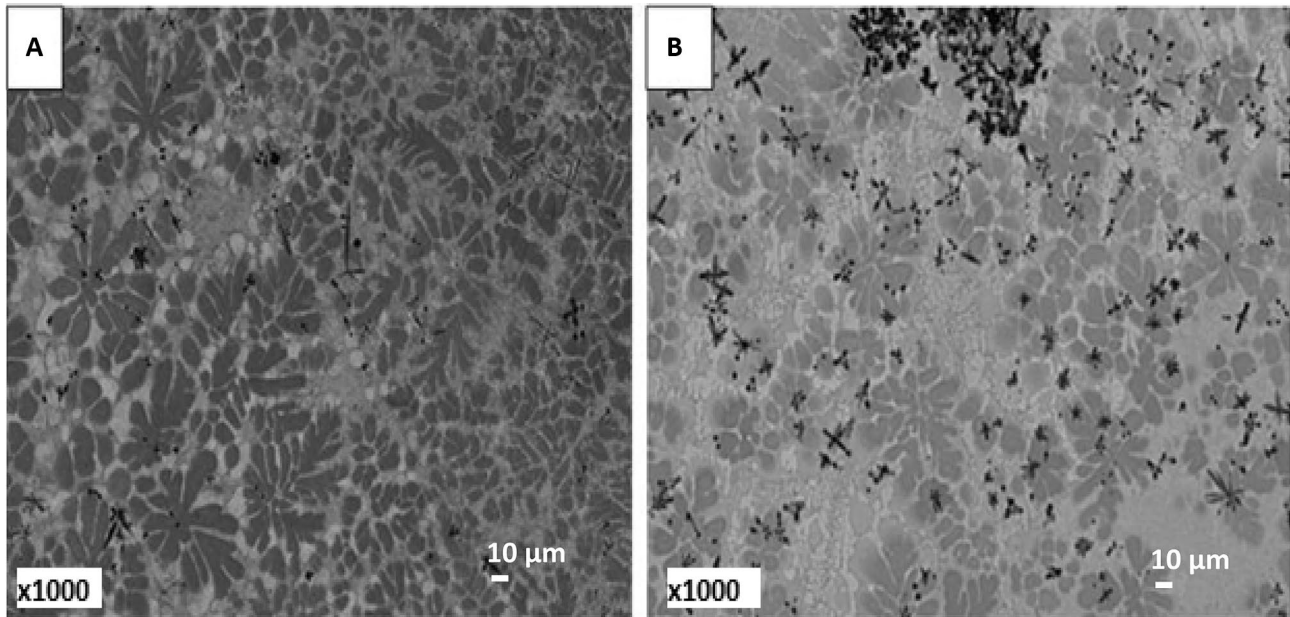**Fig. 5** Microstructure of the Ti–Co–10Ni Coatings at **a** 0.6 m/min and **b** 1.2 m/min

Fig. 6 SEM micrographs of Co–Ni–10Ti coatings at **a** 0.6 m/min and **b** 1.2 m/min
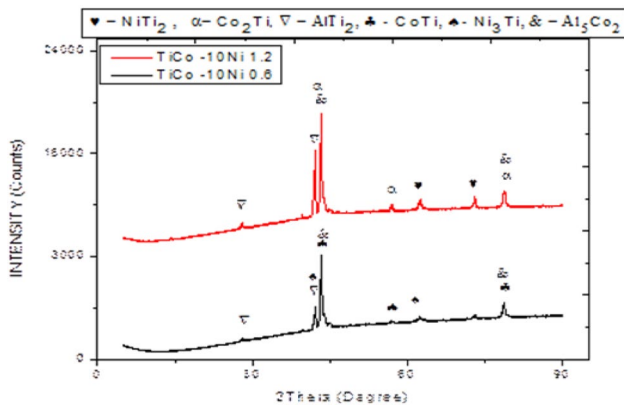

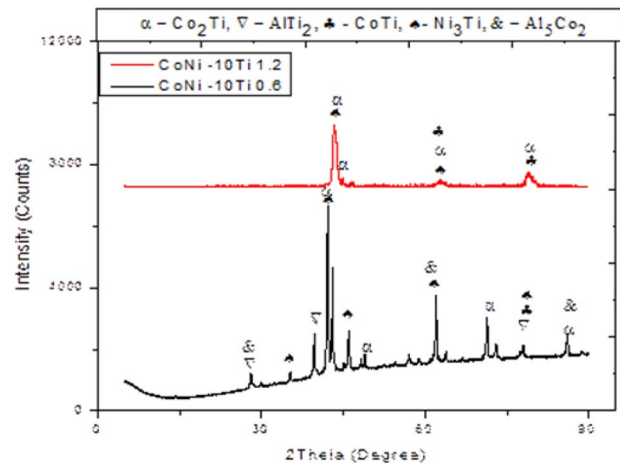**Fig. 7** XRD image of Ti–Co–10Ni coated sample at 0.6 m/min and 1.2 m/min

Fig. 8 XRD image of Co–Ni–10Ti coated sample at 0.6 m/min and 1.2 m/min

admixture affect the intermetallic phases that were formed. At diffraction angles, the deposition of Ti–Co–10Ni ternary for the XRD at varying scan speeds were observed as illustrated in Fig. 7. The peaks reveal $AlTi_2$, $NiTi_2$, Ni_3Ti, Ti–Co, Co_2Ti, and Al_5O_2 phases. $AlTi_2$, Al_5O_2, Ni_3Ti, and Ti–Co are the visible diffraction peaks of coatings deposited at 0.6 m/min scan speed; $TiCo_2$ and $NiTi_2$ were present at 1.2 m/min scan speed. Owing to the strong temperature gradients emanating from the melt pool, solidification rate increases at high scan speeds, resulting in the nickel and cobalt phases' development [47, 48]. Furthermore, owing to the longer dwell time of the laser radiation, that is the release of the elongated kinetic energy and the melt pool solidifying,

the occurrence of phases containing titanium and aluminum further clarifies the robustness of the metallurgical relationship between the alloy and the coatings.

The Co–Ni–10Ti ternary intermetallic coatings' XRD patterns (Fig. 8), which were obtained at two distinct scan speeds as earlier stated, show peaks at different diffraction angles. The following phases: Co_2Ti, Ni_3Ti, Al_5Co_2, $AlTi_2$, and Ti–Co are visible. Co_2Ti, Ni_3Ti, Al_5Co_2, $AlTi_2$, and Ti–Co were the main intermetallic pikes that deposited at 0.6 m/min, whereas Ni_3Ti, Ti–Co, and Co_2Ti intermetallic stages dominated the cladding at 1.2 m/min speed.

Adequate shielding during the laser cladding procedure prevented the creation of any metallic oxides including cobalt, nickel, or titanium oxides. According to Weng et al. [39], complex chemical reactions are produced when there is interaction between the molten powders and the substrate due to the high energy emitted by the laser beam. Ni_3Ti, Co_2Ti, and Ti–Co, significant hard phases required for superior mechanical and wear resistance, were produced during the fusion of the Co, Ti, and Ni mixed portion [30, 33, 36, 42, 43, 49]. The presence of $AlTi_2$ was also observed in Fig. 8. According to Kaibyshev et al. [50], an essential factor in the creation of the aluminum-rich aluminum-titanium phase ($AlTi_2$) is the adding of titanium to serve as a grain refiner. This $AlTi_2$ phase increases the strengthening effect of the coating, lowers the tendency of porosity in the melt pool, and increases tensile intensities. [51, 52].

3.4 Characterization of the Microhardness of the Laser Coatings

Figure 9 and Table 3 show the outcomes of the analysis of the microhardness data of the coatings of Co–Ni–10Ti and Ti–Co–10Ni on the substrate. As scan speed increases, the hardness of the ternary coatings varies, while the hardness in Ti–6Al–4V remains constant at 334 HV. Higher scan speeds, particularly with the Co–Ni–10Ti composition, resulted in a significant increase in microhardness. Microhardness values were found to be 756 $HV_{0.1}$ and 791 $HV_{0.1}$ at a respective speed of 0.6 and 1.2 m/min for the Ti–Co–10Ni ternary coatings, while at 0.6 and 1.2 m/min speeds, the respective values of microhardness are 904 $VH_{0.1}$ and 977 $HV_{0.1}$ for Co–Ni–10Ti coatings. As shown in Figs. 7 and 8, the existence of hard intermetallic compounds creates strengthening effects within the coatings that lead to the coating's hardness
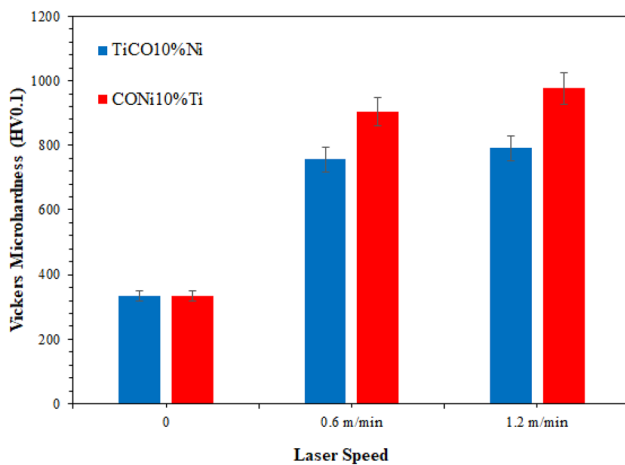
enhancement. Fine grains, which are a sign of a quick heat transition during the solidification process, may be the cause of the microhardness value rising as laser scan speed increases [53, 54]. Furthermore, Fig. 10 illustrates how the ternary coatings' microhardness profiles change with depth. The coating zone, and the transition zone (Heat affected zone (HAZ)), as well as the substrate zone (Ti–6Al–4V), are all visible in the microhardness profile. Due to the substrate's ultra-chilling and dilution effect, the coated zone's microhardness was higher, while there was gradual decrease in the hardness value at the HAZ [9]. The hardness of the deposited alloy is greatly influenced by the deposition process parameters such as temperature, deposition rate, and cooling rate. Variations in these parameters can lead to different microstructural characteristics such as grain size and phase distribution, which affect hardness. Generally, the hardness performance of the Co–Ni–10Ti coating deposited at a scan speed of 1.2 m/min, exhibited a hardness of 980 HV. When compared to the substrate material, Ti–6Al–4V, which has a

Table 3 Surface micro-hardness of Ti–Co–10Ni and Co–Ni–10Ti metallic coatings

Sample	Scan speed (m/min)	Hardness value (HV)
Control (Ti–4Al–4V)		334
Ti–Co–10Ni	0.6	756
Ti–Co–10Ni	1.2	791
Co–Ni–10Ti	0.6	904
Co–Ni–10Ti	1.2	977

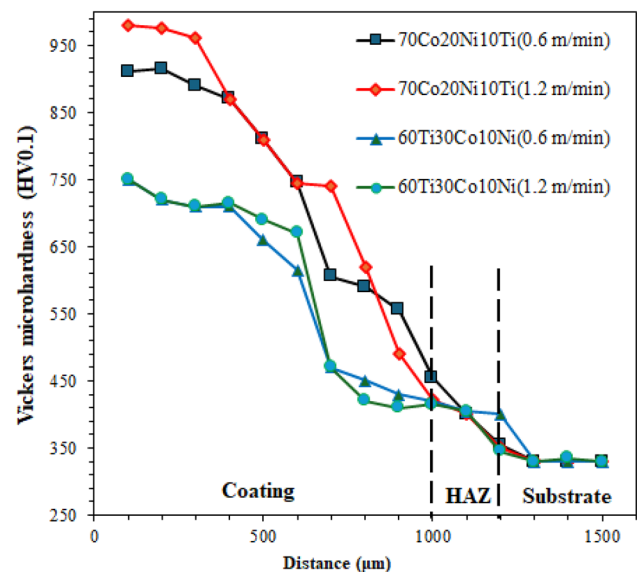**Fig. 9** Surface microhardness chart for ternary coatings of Ti–Co–10Ni and Co–Ni–10Ti

Fig. 10 Microhardness of ternary coatings for Ti–Co–10Ni and Co–Ni–10Ti

hardness of 330 HV, the coating demonstrated a remarkable increase in hardness, approximately 2.96 times greater than the substrate. This significant increase in hardness values indicates the effect of the laser clad Co–Ni–10Ti coating on the base alloy, highlighting its potential for applications requiring enhanced wear resistance and durability.

3.5 Wear Morphology and Mechanism

The wear morphology of the two intermetallic coatings dropped on Ti–6Al–4V as displayed in Figs. 11 and 12. Figure 11A and B display the micrographs of the eroded face of Ti–Co–10Ni cladding at both scan rates. Severe adhesive wear on both coatings revealed smeared worn debris on the surface. Furthermore, Fig. 11A shows that the welded debris obtained from the worn regions has sticked to the coating surface, causing it to become rough on the surface and distorted with ploughing grooves. Additionally, Fig. 11B showed the morphology of the worn surface having clearly visible worn particles adhering to the surface and obvious plastic flow characteristics. A large temperature gradient

created by high energy input that rapidly diminishes due to solidification and creates internal stresses within the coating could cause a high amount of debris [9].

The worn surfaces in Fig. 11C and D show evidence of oxidative wear due to their Ti enrichment and traces of O, as shown by EDS analyses. This suggests that the debris that adheres is worn-out titanium oxide film. According to [55], oxide film formation and destruction on the friction surface result in oxidative wear frequently occurring in addition to adhesive wear. As shown in Fig. 8, the Ni_3Ti phase on the coating, is presumably difficult to withstand wear, and disallowing Ti interaction with O in the formation of oxide film, though this could be disputed. The eroded face, however, indicates the hardness was probably insufficient to withstand tearing off during ploughing. [39] claim that the microstructural characteristics of coatings were critical when assessing the tribological feature of material. Accordingly, the wear property is negatively impacted by the coarse microstructure that low scan speed reveals in Fig. 6.

By contrast, the morphologies of the Co–Ni–10Ti coatings' worn surface with respect to both scan rates
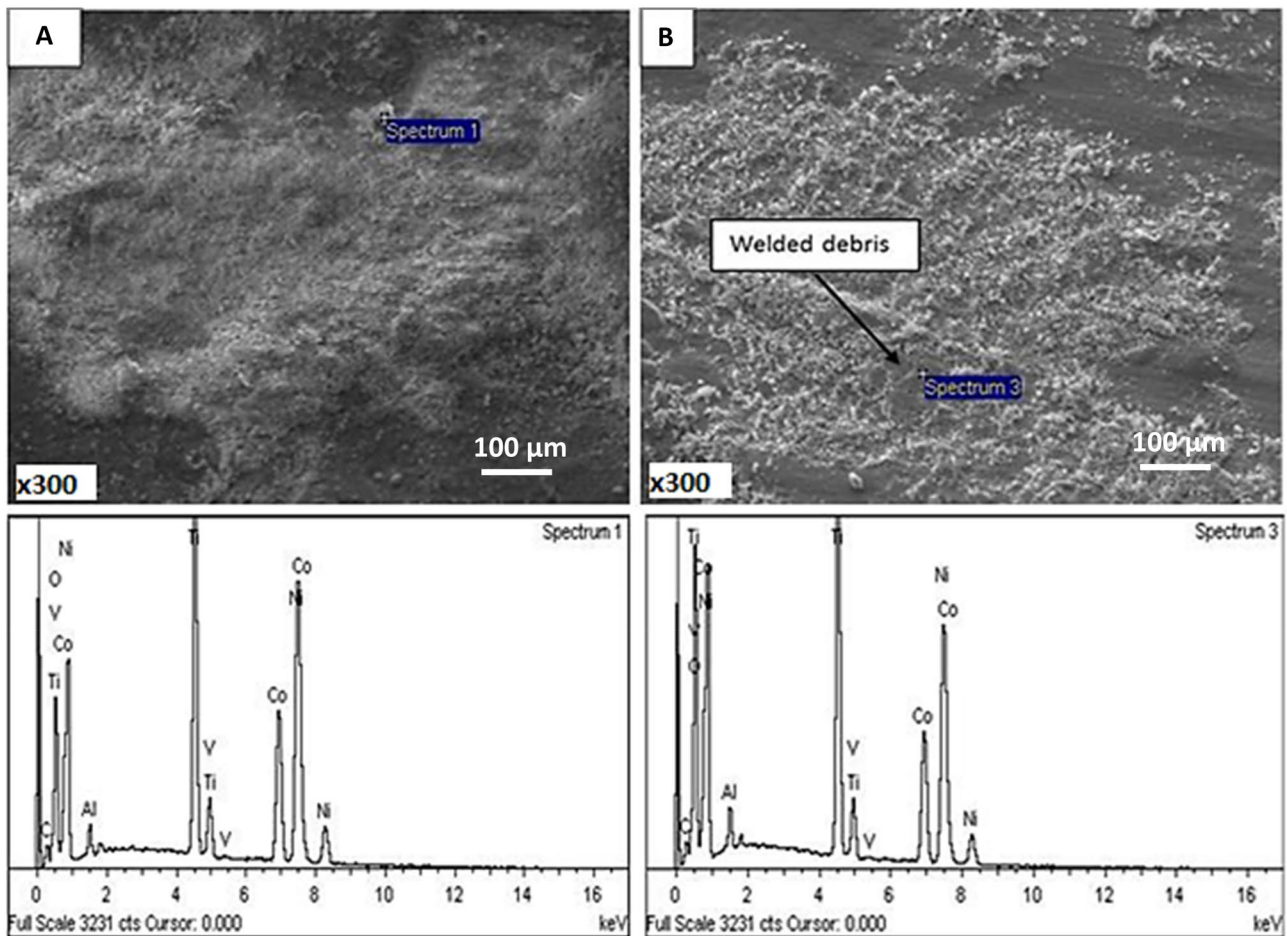

Fig. 11 Morphological wear analysis of laser coated Ti–Co–10Ni ternary coatings at **A** 0.6 m/min and **B** 1.2 m/min
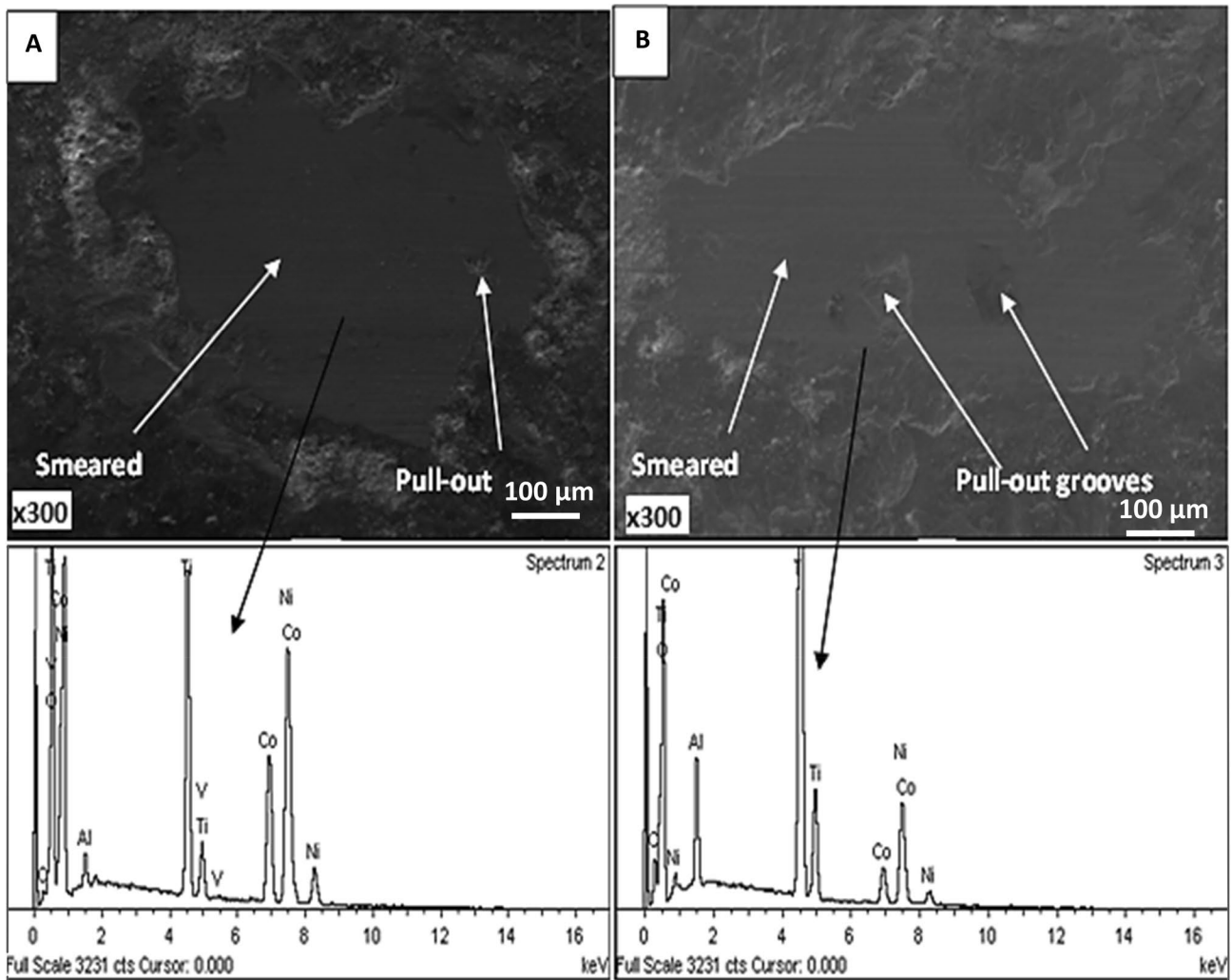
Fig. 12 Morphological wear analysis of laser clad Co–Ni–10Ti ternary coatings at **A** 0.6 m/min and **B** 1.2 m/min

(respectively) are revealed in Fig. 12A and B. The smeared surface and small amount of debris visible in both coatings are characteristics linked to abrasive wear and plastic deformation. Harder surfaces are formed because of the high solidification rate of the melt pool during laser processing, which greatly reduces the amount of time needed for the development of larger grains with a softer matrix. Chen et al. [30] found a similar phenomenon in their work. The steel ball could have hard asperities, causing large pull-out hollows to form on the rough surface (Fig. 12B). The Co–Ni–10Ti coatings' worn surface morphologies are depicted from the EDS analyses (Fig. 12C, D). Adherent worn particles are clearly visible and have distinct plastic flow characteristics. Owing to the increase in temperature at the time of dry sliding wear, the elemental spectrum demonstrates that the wear debris contains elements such as Ni, Ti, Co, and O, suggesting that the debris are primarily worn-out from the titanium alloy.

3.6 Analysis of Frictional Coefficient for Coatings

The frictional coefficients of the steel-clad Ti–Co–10Ni and Co–Ni–10Ti coated in ternary in dry sliding conditions and with a tension of 15 N are shown in Fig. 13. The ternary coatings of were found to have coefficients that were less than the Ti–6Al–4V alloy, which had 1.35 μ mean value. The wear test caused wear debris to form on the ternary coatings, resulting in a reduced coefficient of friction values. Table 4 shows the computed mean data of COF as follows: 0.94 μ and 0.84 μ at 0.6 and 1.2 m/min, respectively, for Ti–Co–10Ni coatings; and 0.69 μ and 0.66 μ at 0.6 and 1.2 m/min, respectively, for Co–Ni–10Ti coating. Figure 11 displays the dominance of massive ploughing grooves and severe plastic deformation on the coating surface, which could be responsible for the high frictional coefficients observed at Ti–Co–10Ni compared to Co–Ni–10Ti. In contrast, the low frictional coefficient observed at the
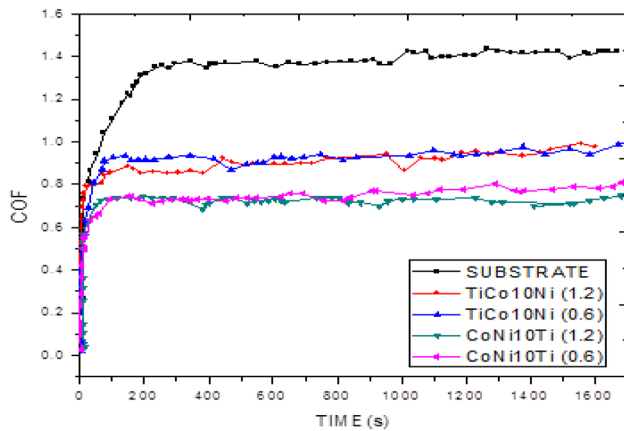
Fig. 13 Frictional coefficients variation with time for ternary coatings

Table 4 Coefficient of friction of ternary coatings

Sample	Scan speed (m/min)	Friction coefficient
Control (Ti–4Al–4V)		1.35 μ
Ti–Co–10Ni	0.6	0.94 μ
Ti–Co–10Ni	1.2	0.84 μ
Co–Ni–10Ti	0.6	0.69 μ
Co–Ni–10Ti	1.2	0.66 μ

Co–Ni–10Ti composition may be due to an increased energy density (Fig. 8), which facilitates the strong adhesion and efficient Co and Ni particle melting to create robust intermetallic phases like Al_5Co_2, Co_2Ti, Ti–Co, and Ni_3Ti. The stable inhibitive layers that these hard intermetallic phases provide to the clad surface have a hardening effect by reducing surface roughness. Due to the lower coefficient of friction caused by the protective intermetallic phases, the wear resistance performance is superior.

4 Conclusion

In this study, the relationship between the substrate and laser-clad coating is metallurgically strong which was successfully developed for the integration of Ti–Co–10Ni and Co–Ni–10Ti ternary coatings.

- The micrograph, hardness value, corrosion behavior, and tribological characteristics of Ti–6Al–4V alloy are significantly influenced by the percentage of laser-clad admixed material and the speed of scanning.

- The Co–Ni–10Ti admixture, 900W laser power, 1.0 g/min powder feed rate, and 1.2 m/min laser velocity were parameters that produced the optimum properties. The phases showed different parts of dispersed interdendritic compounds including Co_2Ti, Ni_3Ti, Ti–Co, Al_5O_2, and $AlTi_2$) in the coating matrix, which may account for the alloy Ti–6Al–4V's (334 HV) 2.9-fold increase in surface hardness.

- The performance of excellent wear resistance is shown by the Co–Ni–10Ti (1.2 m/min) ternary alloy, which has a 51.1% lower frictional coefficient than the Ti–6Al–4V alloy. This reduced friction coefficient may be attributed to the higher energy density attained at the Co–Ni–10Ti composition, which facilitates the strong adhesion and efficient melting of Co and Ni particles in the development of hard intermetallic phases. The intermetallic phases reduce the coefficient of friction, which in turn shows superior tribological behavior.

Author Contributions Authors: Olanrewaju Seun Adesina, Gabriel Ayokunle Farotade, Babatunde Abiodun Obadele and Olufemi Oluseun Sanyaolu designed the study, performed the experiment, interpreted results and wrote the first draft of the manuscript. Authors, Peter Pelumi Ikubanni, Modupe Eunice Sanyaolu, Adeolu Adesoji Adediran and Adekunle Akanni Adeleke managed the analyses of the study, managed literature searches and graphical editing. All authors read and approved the final manuscript.

Data Availability No datasets were generated or analyzed during the current study.

Declarations

Conflict of interest The authors declare no competing interests.

Consent to Participate Not applicable.

Consent for Publication Not applicable.

Ethical Approval Collection of plant material, comply with relevant institutional, national, and international guidelines and legislation.

References

1. Baker TN (2010) 12—Laser surface modification of titanium alloys. In: Dong H (ed) Surface engineering of light alloys. Woodhead publishing series in metals and surface engineering. Woodhead Publishing, Sawston, pp 398–443

2. Banerjee D, Williams JC (2013) Perspectives on titanium science and technology. Acta Mater 61:844–879. https://doi.org/10.1016/j.actamat.2012.10.043

3. Barreda J, Santamarıa F, Azpiroz X, Irisarri A, Varona J (2001) Electron beam welded high thickness Ti6Al4V plates using filler metal of similar and different composition to the base plate. Vacuum 62:143–150. https://doi.org/10.1016/S0042-207X(00)00454-1

4. Budinski KG (1991) Tribological properties of titanium alloys. Wear 151:203–217. https://doi.org/10.1016/0043-1648(91)90249-T

5. Savalani M, Ng C, Li Q, Man H (2012) In situ formation of titanium carbide using titanium and carbon-nanotube powders by laser cladding. Appl Surf Sci 258:3173–3177. https://doi.org/10.1016/j.apsusc.2011.11.058

6. Candel JJ, Jimenez JA, Franconetti P, Amigó V (2014) Effect of laser irradiation on failure mechanism of TiCp reinforced titanium composite coating produced by laser cladding. J Mater Process Technol 214:2325–2332. https://doi.org/10.1016/j.jmatprotec.2014.04.035

7. Chikarakara E, Naher S, Brabazon D (2012) High speed laser surface modification of Ti–6Al–4V. Surf Coat Technol 206:3223–3229. https://doi.org/10.1016/j.surfcoat.2012.01.010

8. Weng F, Chen C, Yu H (2014) Research status of laser cladding on titanium and its alloys: a review. Mater Des 58:412–425. https://doi.org/10.1016/j.matdes.2014.01.077

9. Weng F, Yu H, Chen C, Liu J, Zhao L, Dai J (2016) Microstructure and property of composite coatings on titanium alloy deposited by laser cladding with Co42+TiN mixed powders. J Alloys Compd 686:74–81

10. Razavi RS, Salehi M, Monirvaghefi M, Gordani GR (2008) Corrosion behaviour of laser gas-nitrided Ti–6Al–4V alloy in nitric acid solution. J Mater Process Technol 203:315–320. https://doi.org/10.1016/j.jmatprotec.2007.10.020

11. Turichin G, ZemIyakov E, Babkin K, Ivanov S, Vildanov A (2018) Laser metal deposition of Ti-6Al-4V alloy with beam oscillation. Procedia CIRP 74:184–187. https://doi.org/10.1016/j.procir.2018.08.090

12. Klimova-Korsmik O, Turichin G, Zemlyakov E, Babkin K (2016) Technology of high-speed direct laser deposition from Ni-based superalloys. Phys Procedia 83:716–722. https://doi.org/10.1016/j.phpro.2016.08.073

13. Lewandowski JJ, Seifi M (2016) Metal additive manufacturing: a review of mechanical properties. Annu Rev Mat Res 46:151–186. https://doi.org/10.1146/annurev-matsci-070115-032024

14. Fellah M, Labaïz M, Assala O, Dekhil L, Taleb A, Rezag H, Iost A (2014) Tribological behavior of Ti-6Al-4V and Ti-6Al-7Nb alloys for total hip prosthesis. Adv Tribol 13:451387. https://doi.org/10.1155/2014/451387

15. Zhang Y, Qu J, Wang H (2016) Wear characteristics of metallic counterparts under elliptical-locus ultrasonic vibration. Appl Sci 6:289. https://doi.org/10.3390/app6100289

16. Adebiyi DI, Popoola API (2015) Mitigation of abrasive wear damage of Ti–6Al–4V by laser surface alloying. Mater Des 74:67–75. https://doi.org/10.1016/j.matdes.2015.02.010

17. Bansal DG, Eryilmaz OL, Blau PJ (2015) Surface engineering to improve the durability and lubricity of Ti–6Al–4V alloy. Wear 271:2006–2015. https://doi.org/10.1016/j.wear.2010.11.021

18. Bloyce A, Qi PY, Dong H, Bell T (1998) Surface modification of titanium alloys for combined improvements in corrosion and wear resistance. Surf Coat Technol 107:125–132. https://doi.org/10.1016/S0257-8972(98)00580-5

19. Majumdar JD, Manna I (2015) 21—Laser surface engineering of titanium and its alloys for improved wear, corrosion and high-temperature oxidation resistance. In: Waugh JLG (ed) Laser surface engineering. Woodhead publishing series in metals and surface engineering. Woodhead Publishing, Sawston, pp 483–521. https://doi.org/10.1016/B978-1-78242-074-.00021-0

20. Yang M-S, Liu X-B, Fan J-W, He X-M, Shi S-H, Fu G-Y, Wang M-D, Chen S-F (2012) Microstructure and wear behaviors of laser clad NiCr/Cr_3C_2–WS_2 high temperature self-lubricating wear-resistant composite coating. Appl Surf Sci 258:3757–3762. https://doi.org/10.1016/j.apsusc.2011.12.021

21. Huang SW, Nolan D, Brandt M (2003) Pre-placed WC/Ni clad layers produced with a pulsed Nd:YAG laser via optical fibres. Surf Coat Technol 165:26–34. https://doi.org/10.1016/S0257-8972(02)00700-4

22. Adesina O, Popoola P, Fatoba O (2016) Laser surface modification—a focus on the wear degradation of titanium alloy. InTech Open. https://doi.org/10.5772/61737

23. Nassar AR, Keist JS, Reutzel EW, Spurgeon TJ (2015) Intra-layer closed-loop control of build plan during directed energy additive manufacturing of Ti–6Al–4V. Addit Manuf 6:39–52. https://doi.org/10.1016/j.addma.2015.03.005

24. Tang L, Landers RG (2010) Melt pool temperature control for laser metal deposition processes—part II: layer-to-layer temperature control. J Manuf Sci Eng Trans 132:011011. https://doi.org/10.1115/1.4000883

25. Wang L, Felicelli SD, Craig JE (2007) Thermal modeling and experimental validation in the lens™ process. In: Proceedings of 12th Solid Free. Fabr. Symp., pp 100–111. https://utw10945.utweb.utexas.edu/Manuscripts/2007/2007-09-Wang.pdf

26. Garrett J, Marshall W, Joseph Y, Scott M et al (2016) Understanding the microstructure formation of Ti-6Al-4V during direct laser deposition via in-situ thermal monitoring. Min Metals Mat Soc 68:778–790. https://doi.org/10.1007/s11837-015-1767-z

27. Neela V, De A (2009) Three-dimensional heat transfer analysis of LENSTM process. Int J Adv Manuf Technol 45:935–943. https://doi.org/10.1007/s00170-009-2024-9

28. Bakhit B, Akbari A, Nasirpouri F, Hosseini MG (2014) Corrosion resistance of Ni–Co alloy and Ni–Co/SiC nanocomposite coatings electrodeposited by sediment codeposition technique. Appl Surf Sci 307:351–359. https://doi.org/10.1016/j.apsusc.2014.04.037

29. Langelier BC, Esmaeili S (2009) In-situ laser-fabrication and characterization of TiC-containing Ti–Co composite on pure Ti substrate. J Alloys Compd 482:246–252

30. Xue Y, Wang HM (2009) Microstructure and dry sliding wear resistance of CoTi intermetallic alloy. Intermetallics 17:89–97. https://doi.org/10.1016/j.intermet.2008.06.010

31. Qin R, Zhang X, Guo S, Sun B, Tang S, Li W (2016) Laser cladding of high Co–Ni secondary hardening steel on 18Cr2Ni4WA steel. Surf Coat Technol 285:242–248. https://doi.org/10.1016/j.surfcoat.2015.11.032

32. Obadele BA, Masuku ZH, Olubambi PA (2012) Turbula mixing characteristics of carbide powders and its influence on laser processing of stainless steel composite coatings. Powder Technol 230:169–182. https://doi.org/10.1016/j.powtec.2012.07.025

33. Adesina OS, Mthisi A, Popoola API (2016) The effect of laser based synthesized Ti-Co coating on microstructure and mechanical properties of Ti6Al4V alloy. Proc Manuf 7:46–52. https://doi.org/10.1016/.promfg.2016.12.014

34. Sun Y, Hao M (2012) Statistical analysis and optimization of process parameters in Ti6Al4V laser cladding using Nd:YAG laser.

Optics Lasers Eng 50:985–995. https://doi.org/10.1016/j.optlaseng.2012.01.018

35. Frenk A, Henchoz N, Kurz W (1993) Laser cladding of a cobalt-based alloy: processing parameters and microstructure. Z Metallkd 84:886–892

36. Chunyan L, Song Z, Yuping K, ChangSheng L (2002) Comment on material system for laser cladding. Laser J 23:5–9

37. Alemohammad H, Esmaeili S, Toyserkani E (2007) Deposition of Co–Ti alloy on mild steel substrate using laser cladding. Mater Sci Eng A 456:156–161. https://doi.org/10.1016/j.msea.2006.12.054

38. Chen J-M, Guo C, Zhou J-S (2012) Microstructure and tribological properties of laser cladding Fe-based coating on pure Ti substrate. Trans Nonferr Metals Soc China 22:2171–2178. https://doi.org/10.1016/S1003-6326(11)61445-3

39. Weng F, Yu H, Chen C, Dai J (2015) Microstructures and wear properties of laser cladding Co-based composite coatings on Ti–6Al–4V. Mater Des 80:174–181. https://doi.org/10.1016/j.matdes.2015.05.005

40. Weng F, Yu H, Chen C, Liu J, Zhao L, Dai J, Zhao Z (2017) Effect of process parameters on the microstructure evolution and wear property of the laser cladding coatings on Ti-6Al-4V alloy. J Alloys Compd 692:989–996. https://doi.org/10.1016/j.jallcom.2016.09.071

41. Villars P, Okamoto H, Cenzual K (2006) ASM alloy phase diagrams database. ASM International, Materials Park

42. Davydov AV, Kattner UR, Josell D, Waterstrat RM, Boettinger WJ, Blendell JE, Shapiro AJ (2001) Determination of the CoTi congruent melting point and thermodynamic reassessment of the Co-Ti system. Metall Mat Trans A 32:2175–2186. https://doi.org/10.1007/s11661-001-0193-8

43. Anada S, Zensho A, Yasuda H, Mori H (2016) Phase change of CoTi and Co_3Ti induced by MeV-scale electron irradiation. Phil Mag 96:2027–2039. https://doi.org/10.1080/14786435.2016.1185187

44. Cai B, Tan Y-F, Tu Y-Q, Wang X-L, Tan H (2011) Tribological properties of Ni-base alloy composite coating modified by both graphite and TiC particles. Trans Nonferr Metals Soc China 21:2426–2432. https://doi.org/10.1016/S1003-6326(11)61031-5

45. Liu R, Xi S, Kapoor S, Wu X (2010) Effects of chemical composition on solidification, microstructure and hardness of Co-Cr-W-Ni and Co-Cr-Mo-Ni alloy systems. Int J Res Rev Appl Sci 5:110–122

46. Shuja SZ, Yilbas BS (2011) Laser produced melt pool: influence of laser intensity parameter on flow field in melt pool. Opt Laser Technol 43:767–775. https://doi.org/10.1016/j.optlastec.2010.12.003

47. Gao F, Wang H (2008) Effect of TiNi in dry sliding wear of laser melt deposited Ti2Ni/TiNi alloys. Mater Charact 59:1349–1354. https://doi.org/10.1016/j.matchar.2008.05.007

48. Gordani GR, ShojaRazavi R, Hashemi SH, Isfahani ARN (2008) Laser surface alloying of an electroless Ni–P coating with Al-356 substrate. Opt Lasers Eng 46:550–557. https://doi.org/10.1016/j.optlaseng.2008.02.002

49. Cai F, Jiang C, Fu P, Ji V (2015) Effects of Co contents on the microstructures and properties of electrodeposited NiCo–Al composite coatings. Appl Surf Sci 324:482–489. https://doi.org/10.1016/j.apsusc.2014.10.159

50. Kaibyshev R, Mazurina I, Gromov D (2006) Mechanisms of grain refinement in aluminum alloys in the process of severe plastic deformation. Metal Sci Heat Treat 48:57–62. https://doi.org/10.1007/s11041-006-0044-8

51. Liu X, Warren AP, Nuhfer NT, Rollett AD, Coffey KR, Barmak K (2014) Comparison of crystal orientation mapping-based and image-based measurement of grain size and grain size distribution in a thin aluminum film. Acta Mater 79:138–145. https://doi.org/10.1016/j.actamat.2014.07.014

52. Fleischer R, Dimiduk D, Lipsitt H (1989) Intermetallic compounds for strong high-temperature materials: status and potential. Annu Rev Mat Sci 19:231–263. https://doi.org/10.1146/annurev.ms.19.080189.001311

53. Emamian A, Corbin SF, Khajepour A (2011) The influence of combined laser parameters on in-situ formed TiC morphology during laser cladding. Surf Coat Technol 206:124–131. https://doi.org/10.1016/j.surfcoat.2011.06.062

54. Mahamood RM, Akinlabi ET, Shukla M, Pityana S (2013) Scanning velocity influence on microstructure, microhardness and wear resistance performance of laser deposited Ti6Al4V/TiC composite. Mater Des 50:656–666. https://doi.org/10.1016/j.matdes.2013.03.049

55. Dehm G, Balk TJ, Edongué EA (2003) Small-scale plasticity in thin Cu and Al films. Microelectron Eng 70:412–424. https://doi.org/10.1016/S0169-9317(03)00395-2